Lattice dynamics of orthorhombic $NdGaO_3$

A. Mock,[1,2,*] R. Korlacki,[2] S. Knight,[2] M. Stokey,[2] A. Fritz,[2] V. Darakchieva,[1] and M. Schubert[1,2,3]

[1]*Terahertz Materials Analysis Center and Competence Center for III-Nitride Technology C3NiT - Janzén, Department of Physics, Chemistry, and Biology (IFM), Linköping University, SE 58183 Linköping, Sweden*

[2]*Department of Electrical and Computer Engineering, University of Nebraska, Lincoln, Nebraska 68588, USA*

[3]*Leibniz Institute for Polymer Research, 01069 Dresden, Germany*

(Received 18 February 2019; published 17 May 2019)

A complete set of infrared-active and Raman-active lattice modes is obtained from density functional theory calculations for single-crystalline centrosymmetric orthorhombic neodymium gallate. The results for infrared-active modes are compared with an analysis of the anisotropic long-wavelength properties using generalized spectroscopic ellipsometry. The frequency-dependent dielectric function tensor and dielectric loss function tensor of orthorhombic neodymium gallium oxide are reported in the spectral range of 80–1200 cm^{-1}. A combined eigendielectric displacement vector summation and dielectric displacement loss vector summation approach augmented by considerations of lattice anharmonicity is utilized to describe the experimentally determined tensor elements. All infrared-active transverse and longitudinal optical mode pairs obtained from density functional theory calculations are identified by our generalized spectroscopic ellipsometry investigation. The results for Raman-active modes are compared to previously published experimental observations. Static and high-frequency dielectric constants from theory as well as experiment are presented and discussed in comparison with values reported previously in the literature.

DOI: 10.1103/PhysRevB.99.184302

I. INTRODUCTION

Neodymium gallate ($NdGaO_3$) belongs to the family of orthorhombic rare-earth perovskites. $NdGaO_3$ has garnered much interest as a substrate material for epitaxial growth; for example GaN layers on $NdGaO_3$ have been investigated for optical applications [1,2]. As such, investigations into the optical and electronic properties have been conducted. For example, Reshak *et al.* performed density functional theory calculations of the electronic band dispersion, density of states, and optical transitions in neodymium gallate and compared results with spectroscopic ellipsometry measurements in the vacuum ultraviolet spectral range [3]. A wide indirect band gap of about 3.8 eV with valence band maximum at T and conduction band minimum at Γ points within the Brillouin zone was found [3]. The lattice dynamics of $NdGaO_3$ have been the subject of numerous studies. The lattice mode structure of orthorhombic $NdGaO_3$ includes infrared-active, Raman-active, and silent modes, where all infrared-active modes split into transverse optical and longitudinal optical modes. Both experimental as well as theoretical (rigid ion and shell model approximations) studies have been reported, but no first-principles calculations have been performed so far. Furthermore, the agreement between reported results remains unsatisfactory. Earlier studies often did not take into account the optical anisotropy of the orthorhombic crystal. For example, in some studies, infrared-active modes are identified without clear description of the polarization orientation [4–6]. Zhang *et al.* performed reflectance and transmittance measurements on the surface of (100)-oriented single-crystal $NdGaO_3$ without specification of the polarization conditions [7]. The authors used an eigendielectric displacement summation approach and report transverse optical lattice mode parameters without symmetry assignment. Saine *et al.* performed unpolarized infrared and Raman spectroscopy measurements, and performed an analysis of the interatomic force field but assumed a different crystal symmetry ($Pbn2_1$) [8]. Suda *et al.* presented polarized infrared reflectance data in the spectral region of 100–600 cm^{-1}, measured with polarization of the incident beam along the three principal directions. However, the set of experimentally identified infrared-active lattice modes remained incomplete, and the longitudinal optical lattice modes were not reported [9]. A detailed study of the polarized infrared reflectance was performed by Höfer *et al.* by investigation of light polarized along the three principal crystallographic directions. Höfer *et al.* identified and reported a set of transverse optical and longitudinal optical lattice modes for the three major crystal directions. However, the set remained incomplete [10].

Raman-active lattice modes in $NdGaO_3$ were studied by many groups [5,9,11,12]. Kamishima *et al.* and Suda *et al.* presented Raman scattering spectra of $NdGaO_3$ as a function of temperature [9,12]. Suda *et al.* also provide a comprehensive review of all previously observed infrared-active and Raman-active lattice modes. Up to now, all reported sets of Raman-active modes in orthorhombic $NdGaO_3$ remained incomplete. From the available lattice mode information, Suda *et al.* created a rigid ion model for the interatomic force fields in $NdGaO_3$. Suda *et al.* used their rigid ion model and calculated the lattice mode dispersions. The infrared portion of their original study was later refined, resulting in a refined phonon dispersion based on their rigid ion shell model [13]. The lattice mode dispersions provided by Suda *et al.*

*amock@huskers.unl.edu; http://ellipsometry.unl.edu

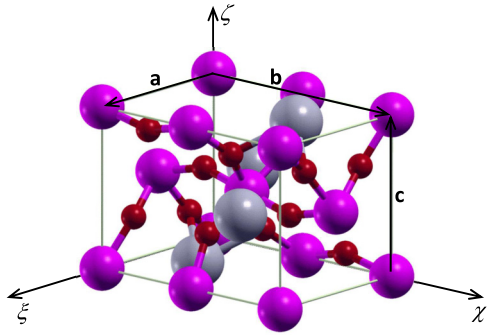

FIG. 1. Unit cell of $NdGaO_3$ with crystallographic vectors **a**, **b**, and **c** defined with relation to the orthogonal coordinate system (ξ, χ, ζ).

[9,13], however, suffer from the fact that neither the set of infrared-active nor the set of Raman-active lattice modes was observed completely, and no information on the silent modes is available thus far. Furthermore, the rigid ion model suffers from ignoring the quantum mechanical nature of the atomic interactions. Hence, the rigid ion model is known to only serve as a crude approximation of the lattice dynamics of crystals.

In this paper, we present a comprehensive study of the phonon modes in $NdGaO_3$. All phonon modes are calculated from first principles using density functional theory (DFT). The results for infrared-active modes are compared with a detailed and complete analysis of the anisotropic long-wavelength properties using generalized spectroscopic ellipsometry (GSE). The frequency-dependent dielectric function tensor and dielectric loss function tensor of orthorhombic neodymium gallium oxide is reported in the spectral range of 80–1200 cm^{-1}. A combined eigendielectric displacement vector summation and dielectric displacement loss vector summation approach augmented by considerations of lattice anharmonicity is utilized to describe the experimentally determined tensor elements. All infrared-active transverse and longitudinal optical mode pairs obtained from density functional theory calculations are identified by our generalized spectroscopic ellipsometry investigation and found in excellent agreement. The results for Raman-active modes are compared to previously published experimental observations. Static and high-frequency dielectric constants from theory as well as experiment are presented and discussed in comparison with values reported previously in the literature. Frequencies of all silent lattice modes are presented as well. We show the atomic displacement patterns for all phonon modes and plot the phonon dispersion based on the DFT calculated interatomic force field.

TABLE I. Comparison between the experimental and theoretical lattice constants (in Å). Literature data have been converted to the *Pnma* cell used in the present study.

	Exp.[a]	Exp.[b]	Exp.[c]	Calc.[d]
a	5.499	5.4952	5.4979	5.4443
b	7.733	7.6871	7.7078	7.6369
c	5.431	5.4176	5.4276	5.3805

[a]Ref. [25]; [b]100 K, Ref. [18]; [c]293 K, Ref. [18]; [d]This work, LDA-DFT.

TABLE II. Calculated equilibrium structural parameters of $NdGaO_3$ determined in this work in comparison with available literature values. Atomic positions are given in fractional coordinates of **a**, **b**, and **c**, respectively. Literature data have been converted to the *Pnma* cell used in the present study.

Exp. (100 K, Ref. [18])			
Nd	0.04268	0.25	0.49087
Ga	0	0.5	0
O1	0.0181	0.75	0.0803
O2	0.2092	0.5426	0.7098
Exp. (293 K, Ref. [18])			
Nd	0.04141	0.25	0.49092
Ga	0	0.5	0
O1	0.0174	0.75	0.0800
O2	0.2097	0.5422	0.7107
Calc. (this work)			
Nd	0.04312	0.25	0.48910
Ga	0	0.5	0
O1	0.0166	0.75	0.0802
O2	0.2136	0.5436	0.7146

II. THEORY

A. Symmetry, coordinate system, and crystal structure

$NdGaO_3$ has orthorhombic crystal structure and belongs to space group No. 62 (*Pnma*) with orthogonal crystal vectors **a**, **b**, and **c** (Fig. 1). The lattice parameters and atomic positions of symmetry-unique atoms within the unit cell are provided in Tables I and II. Because many previous studies on $NdGaO_3$ used the *Pbnm* cell for identification, even if sometimes indicated otherwise [10], in all places where we compare our results with the literature, for the sake of consistency we convert the literature data given in the *Pbnm* to the *Pnma* cell, with **b** having the longest unit cell dimension. The unit cell contains four chemical units, which results in 20 atoms and 60 zone-center phonon modes classified according to the irreducible representation:

$$\Gamma = 7A_g + 5B_{1g} + 5B_{2g} + 7B_{3g} + 8A_u + 10B_{1u} + 10B_{2u} + 8B_{3u}.$$

TABLE III. Character table for the *Pnma* cell used in the present study. Symmetry elements: Identity E, twofold rotation axes C_{2j}, inversion I, mirror planes σ_j, with $j = \zeta, \xi, \chi$.

	E	$C_{2\zeta}$	$C_{2\xi}$	$C_{2\chi}$	I	σ_ζ	σ_ξ	σ_χ
A_g	1	1	1	1	1	1	1	1
B_{1g}	1	1	−1	−1	1	1	−1	−1
B_{2g}	1	−1	1	−1	1	−1	1	−1
B_{3g}	1	−1	−1	1	1	−1	−1	1
A_u	1	1	1	1	−1	−1	−1	−1
B_{1u}	1	1	−1	−1	−1	−1	1	1
B_{2u}	1	−1	1	−1	−1	1	−1	1
B_{3u}	1	−1	−1	1	−1	1	1	−1

TABLE IV. Parameters of TO and LO phonon modes with B_{2u} symmetry oriented along the crystallographic **a** axis determined by GSE analysis as well as those obtained from density functional theory calculations in comparison with the literature. The last digit is determined with 90% confidence, which is indicated with parentheses for each parameter. Literature data have been converted to the *Pnma* cell used in the present study.

Parameter	$l=1$	2	3	4	5	6	7	8	9
$A^{B_{2u}}_{\mathrm{TO},l}$ (cm^{-1})	28(8)	18(3)	18(4)	32(7)	58(3)	61(5)	28(8)	398.(8)	13(1)[a]
$\omega^{B_{2u}}_{\mathrm{TO},l}$ (cm^{-1})	573.(3)	538.(9)	428.(4)	314.(6)	293.7(0)	277.3(8)	240.3(7)	172.7(4)	116.0(6)[a]
$\gamma^{B_{2u}}_{\mathrm{TO},l}$ (cm^{-1})	28.(9)	6.(6)	8.(6)	11.(5)	6.3(8)	5.9(2)	5.1(6)	3.4(7)	3.6(4)[a]
$\Gamma^{B_{2u}}_{\mathrm{TO},l}$ (cm^{-1})	(0)	−0.0(2)	0.0(4)	0.12(7)	−0.08(6)	−0.17(2)	0.11(7)	−0.0008(1)	0.0(2)[a]
$A^{B_{2u}}_{\mathrm{LO},l}$ (cm^{-1})	222.(6)	54.(5)	108.(4)	33.(0)	6.4(9)	5.5(2)	7.2(8)	14.5(2)	4.5(7)[a]
$\omega^{B_{2u}}_{\mathrm{LO},l}$ (cm^{-1})	651.8(5)	551.7(1)	505.1(4)	420.32	310.(9)	285.8(3)	244.8(1)	189.6(0)	118.6(2)[a]
$\gamma^{B_{2u}}_{\mathrm{LO},l}$ (cm^{-1})	21.4(5)	14.(5)	7.2(6)	9.(2)	13.(8)	7.1(3)	2.7(9)	3.7(5)	3.(6)[a]
$\Gamma^{B_{2u}}_{\mathrm{LO},l}$ (cm^{-1})	0.006(5)	−0.027(2)	−0.003(4)	0.000(9)	0.000(6)	0.0005(4)	0.0037(6)	−0.0008(1)	0.000(2)[a]
$A^{B_{2u}}_{\mathrm{TO},l}$ [(D/Å)^2/amu]	11.11	4.502	3.771	12.96	41.70	37.46	9.980	10.49	0.7395
$\omega^{B_{2u}}_{\mathrm{TO},l}$ (cm^{-1})	572.34	527.12	431.31	318.17	297.33	282.00	244.80	182.59	124.41
$A^{B_{2u}}_{\mathrm{LO},l}$ [(D/Å)^2/amu]	95.89	8.758	24.51	2.951	0.0879	0.0631	0.1258	0.3057	0.0259
$\omega^{B_{2u}}_{\mathrm{LO},l}$ (cm^{-1})	645.12	542.28	492.25	423.03	314.56	289.05	249.48	192.28	125.49
$\omega^{B_{2u}}_{\mathrm{TO},l}$ (cm^{-1}) (Ref. [10])[b,c,d]	574.7	539.1	427.2	312.5	293.7	276.9	240.5	173	116.0
$A^{B_{2u}}_{\mathrm{TO},l}$ (cm^{-1}) (Ref. [10])[b]	279.4	166.1	178.3	418.0	518.7	551.7	251.4	368.8	104.7
$\omega^{B_{2u}}_{\mathrm{LO},l}$ (cm^{-1}) (Ref. [10])[b]	653.1	551.6	505.2	420.7	307.9	283.9	244.3	189.3	117.5
$\omega^{B_{2u}}_{\mathrm{TO},l}$ (cm^{-1}) (Ref. [13])[b]	595	545	424	356	321	290	260	174	

[a]Fit performed by keeping all other phonon mode parameters constant and by selecting small spectral range near lattice mode.
[b]Determined from reflectance measurements.
[c]Average value of the two model approaches used in Ref. [10].
[d]Note that Ref. [10] also included parameters from an additional oscillator centered near 367.6 cm^{-1}, which does not correspond to any feature identified in this work or predicted by theory. All other parameters associated with this oscillator are omitted here.

TABLE V. Parameters of TO and LO phonon modes with B_{3u} symmetry oriented along the crystallographic **b** axis determined by GSE analysis as well as those obtained from density functional theory calculations in comparison with the literature. The last digit is determined with 90% confidence, which is indicated with parentheses for each parameter. Literature data have been converted to the *Pnma* cell used in the present study.

Parameter	$l=1$	2	3	4	5	6	7
$A^{B_{3u}}_{\mathrm{TO},l}$ (cm^{-1})	300.(0)	6(3)	67(2)	28(6)	58(9)	41(1)	16(3)
$\omega^{B_{3u}}_{\mathrm{TO},l}$ (cm^{-1})	591.(3)	550.(3)	342.0(2)	290.9(7)	269.8(1)	170.8(1)	166.0(3)
$\gamma^{B_{3u}}_{\mathrm{TO},l}$ (cm^{-1})	24.(6)	24.(7)	11.9(3)	4.(8)	4.6(8)	5.7(6)	2.2(7)
$\Gamma^{B_{3u}}_{\mathrm{TO},l}$ (cm^{-1})	0.02(1)	−0.08(2)	0.17(8)	0.00(1)	−0.19(9)	0.01(3)	−0.2(7)
$A^{B_{3u}}_{\mathrm{LO},l}$ (cm^{-1})	212.(0)	52.(4)	136.(1)	21.6(4)	8.6(5)	18.9(3)	1.1(7)
$\omega^{B_{3u}}_{\mathrm{LO},l}$ (cm^{-1})	656.2(3)	552.(3)	528.5(6)	308.(2)	286.1(8)	194.5(1)	166.4(2)
$\gamma^{B_{3u}}_{\mathrm{LO},l}$ (cm^{-1})	18.6(0)	3(3)	10.4(6)	18.(7)	7.(8)	7.(1)	3.6(6)
$\Gamma^{B_{3u}}_{\mathrm{LO},l}$ (cm^{-1})	−0.001(1)	−0.03(9)	−0.001(1)	−0.008(9)	0.006(4)	0.0002(0)	−0.004(6)
$A^{B_{3u}}_{\mathrm{TO},l}$ [(D/Å)^2/amu]	10.85	1.153	43.50	10.99	46.40	13.20	0.5094
$\omega^{B_{3u}}_{\mathrm{TO},l}$ (cm^{-1})	585.27	563.01	354.41	294.00	272.36	185.36	165.99
$A^{B_{3u}}_{\mathrm{LO},l}$ [(D/Å)^2/amu]	84.16	1.205	39.29	1.361	0.1383	0.4515	0.0074
$\omega^{B_{3u}}_{\mathrm{LO},l}$ (cm^{-1})	648.36	565.22	516.83	320.91	288.90	198.72	166.36
$\omega^{B_{3u}}_{\mathrm{TO},l}$ (cm^{-1}) (Ref. [10])[a,b]	594.5		344.5	289.8	271.4	169.8	
$A^{B_{3u}}_{\mathrm{TO},l}$ (cm^{-1}) (Ref. [10])[a]	295.7		664.5	368.2	472.9	472.1	
$\omega^{B_{3u}}_{\mathrm{LO},l}$ (cm^{-1}) (Ref. [10])[a]	659.8		528.1	309.3	285.0	194.9	
$\omega^{B_{3u}}_{\mathrm{TO},l}$ (cm^{-1}) (Ref. [13])[a]	595		321	300	290	174	

[a]Determined from reflectance measurements.
[b]Average value of the two model approaches used in Ref. [10].

TABLE VI. Parameters of TO and LO phonon modes with B_{1u} symmetry oriented along the crystallographic **c** axis determined by GSE analysis as well as those obtained from density functional theory calculations in comparison with the literature. The last digit is determined with 90% confidence, which is indicated with parentheses for each parameter. Literature data have been converted to the *Pnma* cell used in the present study.

Parameter	$l=1$	2	3	4	5	6	7	8	9
$A^{B_{1u}}_{\mathrm{TO},l}$ (cm^{-1})	253.(5)	52.(5)[a]	64(3)	227.(8)[a]	35(1)	60(0)	35(4)	414.(8)	5(7)[a]
$\omega^{B_{1u}}_{\mathrm{TO},l}$ (cm^{-1})	606.4(8)	530.(1)[a]	369.3(7)	351.5(7)[a]	304.9(0)	274.8(5)	253.3(0)	175.0(9)	114.(6)[a]
$\gamma^{B_{1u}}_{\mathrm{TO},l}$ (cm^{-1})	29.(5)	29.(3)[a]	6.7(4)	8.3(6)[a]	9.(0)	5.6(3)	4.9(3)	2.2(0)	3.(3)[a]
$\Gamma^{B_{1u}}_{\mathrm{TO},l}$ (cm^{-1})	−0.004(5)	0.058(7)[a]	0.01(8)	0.19(0)[a]	0.16(3)	−0.18(5)	0.09(0)	−0.13(2)	−0.0(1)[a]
$A^{B_{1u}}_{\mathrm{LO},l}$ (cm^{-1})	207.(1)	140.(4)	36.(0)[a]	7.6(6)[a]	25.3(2)	12.2(6)	6.3(0)	15.1(4)	2.1(0)[a]
$\omega^{B_{1u}}_{\mathrm{LO},l}$ (cm^{-1})	661.2(6)	562.4(1)	528.(7)[a]	354.0(7)[a]	330.(2)	296.(8)	258.2(1)	192.6(4)	115.(1)[a]
$\gamma^{B_{1u}}_{\mathrm{LO},l}$ (cm^{-1})	17.7(2)	11.7(1)	32.(9)[a]	5.8(8)[a]	11.(7)	14.(6)	3.2(9)	6.(2)	3.(4)[a]
$\Gamma^{B_{1u}}_{\mathrm{LO},l}$ (cm^{-1})	0.013(5)	−0.029(7)	0.016(3)[a]	0.0021(1)[a]	−0.005(6)	0.002(6)	0.002(3)	−0.003(9)	−0.000(8)[a]
$A^{B_{1u}}_{\mathrm{TO},l}$ [(D/Å)^2/amu]	6.952	0.2605	53.85	0.5365	6.800	43.12	15.76	12.77	0.0738
$\omega^{B_{1u}}_{\mathrm{TO},l}$ (cm^{-1})	606.99	455.01	384.33	348.77	303.76	279.60	259.14	181.61	121.44
$A^{B_{1u}}_{\mathrm{LO},l}$ [(D/Å)^2/amu]	88.91	47.92	0.0808	0.1316	2.411	0.1582	0.0873	0.4214	0.0027
$\omega^{B_{1u}}_{\mathrm{LO},l}$ (cm^{-1})	656.49	560.73	454.70	349.52	334.90	300.07	263.94	193.94	121.55
$\omega^{B_{1u}}_{\mathrm{TO},l}$ (cm^{-1}) (Ref. [10])[b,c]	607.1		367.2	350.6	303.2	276.5	253.7	175.5	
$A^{B_{1u}}_{\mathrm{TO},l}$ (cm^{-1}) (Ref. [10])[a]	234.6		640.5	189.4	376.6	593.2	300.0	371.7	
$\omega^{B_{1u}}_{\mathrm{LO},l}$ (cm^{-1}) (Ref. [10])[b]	665.1	563.1		354.4	330.5	295.9	257.3	191.4	
$\omega^{B_{1u}}_{\mathrm{TO},l}$ (cm^{-1}) (Ref. [13])[b]	595		356	343	300	273	260	174	

[a]Fit performed by keeping all other phonon mode parameters constant and by selecting small spectral range near lattice mode.
[b]Determined from reflectivity measurements.
[c]Average value of the two model approaches used in Ref. [10].

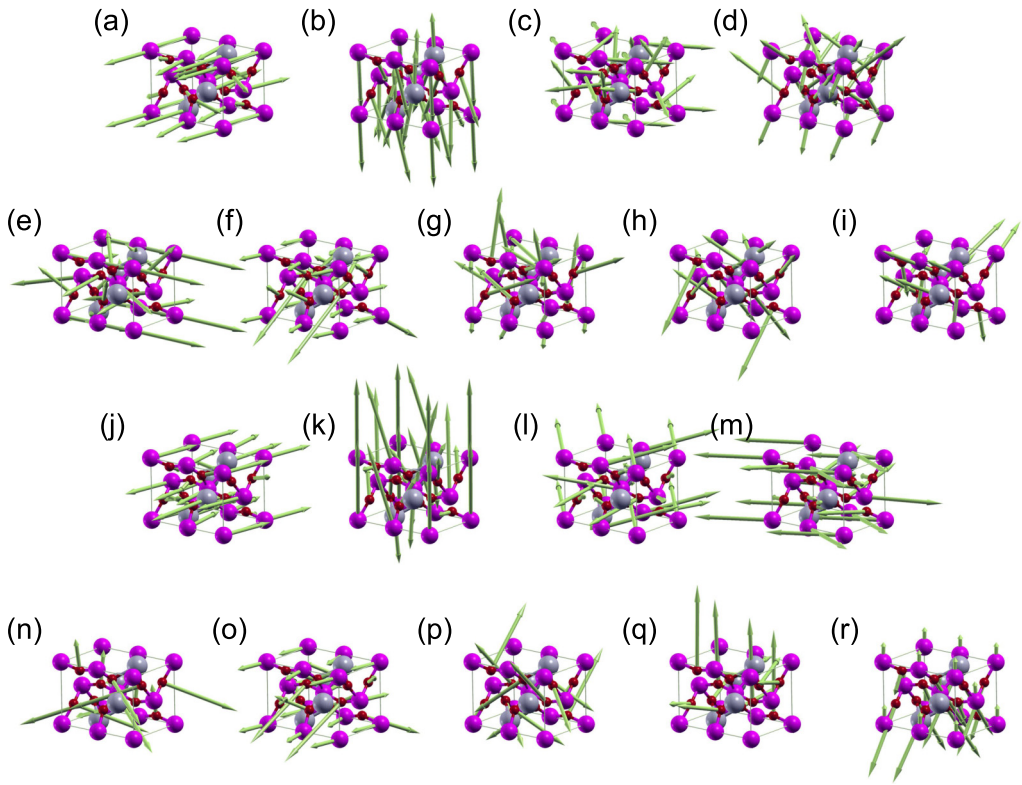

FIG. 2. Phonon modes with B_{1u} symmetry (transition dipoles ∥ **c**) in order of increasing frequency. (a)–(i) TO modes; (j)–(r) LO modes.

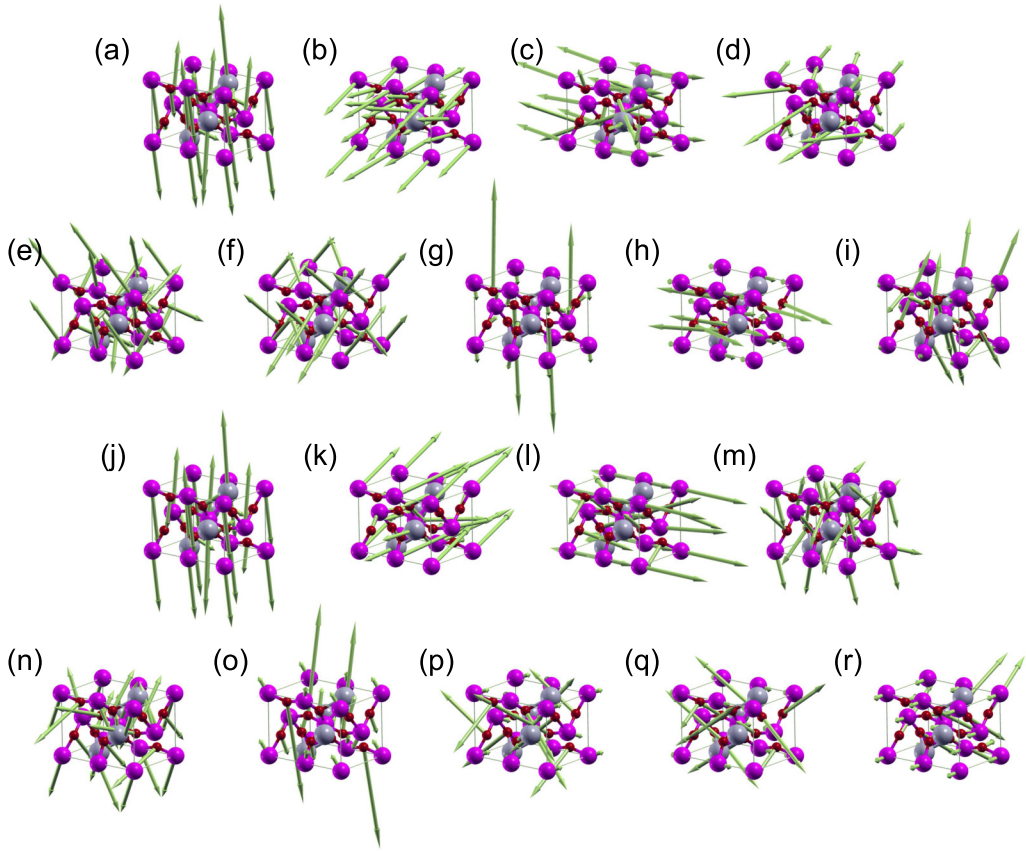

FIG. 3. Phonon modes with B_{2u} symmetry (transition dipoles ∥ **a**) in order of increasing frequency. (a)–(i) TO modes; (j)–(r) LO modes.

One of each B_{1u}, B_{2u}, and B_{3u} are acoustic modes; A_g, B_{1g}, B_{2g}, and B_{3g} are Raman-active modes; A_u modes are silent; and the remaining $9B_{1u}$, $9B_{2u}$, and $7B_{3u}$ modes are active in the infrared. The character table is given in Table III.

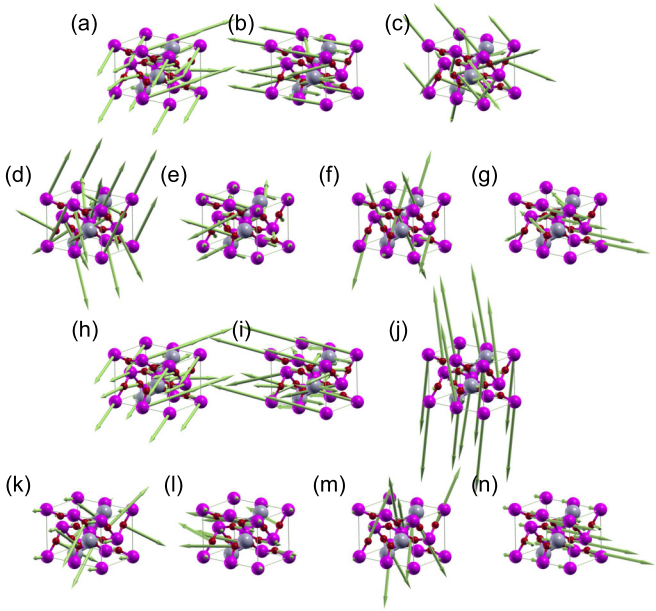

FIG. 4. Phonon modes with B_{3u} symmetry (transition dipoles ∥ **b**) in order of increasing frequency. (a)–(i) TO modes; (j)–(r) LO modes.

B. Density functional theory

Theoretical calculations of long-wavelength-active Γ-point phonon frequencies were performed by plane-wave DFT using QUANTUM ESPRESSO (QE) [14]. We used the local density approximation (LDA) exchange correlation functional of Perdew and Wang (PW) [15] and optimized norm-conserving Vanderbilt (ONCV) scalar-relativistic pseudopotentials [16,17]. The initial parameters of the unit cell and

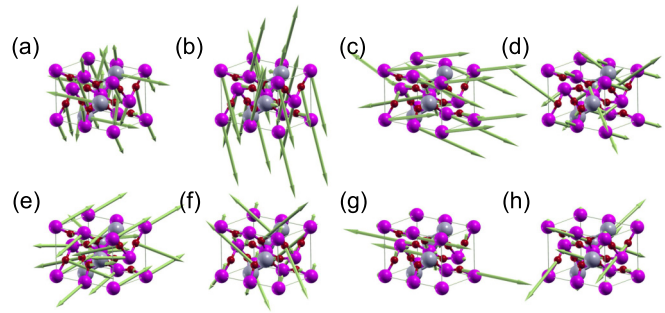

FIG. 5. Phonon modes with A_u symmetry (silent) in order of increasing frequency. DFT-calculated frequencies for these modes are (a) 94.76 cm^{-1}, (b) 170.45 cm^{-1}, (c) 193.88 cm^{-1}, (d) 270.14 cm^{-1}, (e) 296.32 cm^{-1}, (f) 366.78 cm^{-1}, (g) 558.06 cm^{-1}, and (h) 585.84 cm^{-1}.

TABLE VII. Parameters of Raman-active modes with A_g symmetry obtained from density functional theory calculations in comparison with literature. S_{RA} is Raman scattering activity. Mode frequencies of various origins reported in the literature but not corresponding to any expected frequencies were omitted. References given in second column as follows: (a) This work, LDA-DFT; (b) Ref. [5], room temperature; (c) Ref. [11], room temperature; (d) Ref. [12], room temperature; (e) Ref. [12], 21 K; (f) Ref. [9], 31–500 K.

Parameter	Ref.	$l=1$	2	3	4	5	6	7
$S^{A_g}_{RA,l}$ (Å^4/amu)	a	32.94	7.766	16.12	21.34	14.54	1.707	2.040
$\omega^{A_g}_{RA,l}$ (cm^{-1})	a	468.9	421.2	345.4	293.5	232.4	153.4	94.3
$\omega^{A_g}_{RA,l}$ (cm^{-1})	b	470		337	290	215	145	96
$\omega^{A_g}_{RA,l}$ (cm^{-1})	c	469		336	289	214	144	95
$\omega^{A_g}_{RA,l}$ (cm^{-1})	d	470		339	289	215	145	96
$\omega^{A_g}_{RA,l}$ (cm^{-1})	e	474	414	344	297	217	148	104
$\omega^{A_g}_{RA,l}$ (cm^{-1})	f	470	414	339	290	215	145	96

atomic positions were taken from Ref. [18]. The initial structure was first relaxed to force levels less than 10^{-5} Ry bohr^{-1}. A regular shifted $6\times6\times6$ Monkhorst-Pack grid was used for sampling of the Brillouin zone [19]. A convergence threshold of 1×10^{-12} Ry was used to reach self-consistency with a large electronic wave function cutoff of 120 Ry. The relaxed cell was used for subsequent phonon calculations.

The phonon frequencies and eigenvectors were computed at the Γ point of the Brillouin zone using density functional perturbation theory [20]. According to Born and Huang [21], the lattice dynamic properties in crystals are categorized under different electric field **E** and dielectric displacement **D** conditions [22]. Specifically, $\mathbf{E}=0$ and $\mathbf{D}=0$ define the transverse optical (TO) modes, $\omega_{\mathrm{TO},l}$, associated with the dipole moment. $\mathbf{E}\neq0$ but $\mathbf{D}=0$ define the longitudinal optical (LO) modes, $\omega_{\mathrm{LO},l}$. The latter can be obtained using Born effective charges calculated by QE's phonon code [23]. Thus, the parameters of the TO modes were obtained by diagonalizing the dynamic matrix without the electric field effects. The parameters of the LO modes were obtained by adding nonanalytical terms to the dynamic matrix in the respective crystal directions. Hence the DFT calculations yielded 9 phonon mode pairs with polarization along the **a** direction (B_{2u}), 7 pairs along the **b** direction (B_{3u}), and 9 pairs along the **c** direction (B_{1u}), as expected from the irreducible representation of the space group *Pnma*. Amplitudes and frequencies of infrared-active TO and LO phonon modes calculated by DFT are given in Tables IV–VI. Renderings of atomic displacements for these modes were prepared using XCrysDen [24] running under Silicon Graphics Irix 6.5, and are shown in Figs. 2 (B_{1u}), 3 (B_{2u}), 4 (B_{3u}), and 5 (A_u). Additionally, parameters of Raman-active modes are given in Tables VII–X, and the renderings of their atomic displacements are shown in Figs. 6 (A_g), 7 (B_{1g}), 8 (B_{2g}), and 9 (B_{3g}). In addition to the Γ-point phonons, the dynamical matrices were calculated over a regular $8\times8\times8$ grid in the first Brillouin zone. They were used to produce real-space interatomic force constants, which in turn were used to plot the complete phonon dispersion along a high-symmetry path through the first Brillouin zone, shown in Fig. 16.

TABLE VIII. Parameters of Raman-active modes with B_{1g} symmetry obtained from density functional theory calculations in comparison with literature. S_{RA} is Raman scattering activity. Mode frequencies of various origins reported in the literature, but not corresponding to any expected frequencies were omitted. References given in second column as follows: (a) This work, LDA-DFT; (b) Ref. [5], room temperature; (c) Ref. [11], room temperature; (d) Ref. [12], room temperature; (e) Ref. [12], 21 K; (f) Ref. [9], 31–500 K.

Parameter	Ref.	$l=1$	2	3	4	5
$S^{B_{1g}}_{RA,l}$ (Å^4/amu)	a	1.302	3.098	11.99	20.32	0.007
$\omega^{B_{1g}}_{RA,l}$ (cm^{-1})	a	625.5	417.7	361.8	197.8	170.3
$\omega^{B_{1g}}_{RA,l}$ (cm^{-1})	b			351	200	170
$\omega^{B_{1g}}_{RA,l}$ (cm^{-1})	c			349	199	168
$\omega^{B_{1g}}_{RA,l}$ (cm^{-1})	d			351	199	168
$\omega^{B_{1g}}_{RA,l}$ (cm^{-1})	e			355	206	171
$\omega^{B_{1g}}_{RA,l}$ (cm^{-1})	f			351	199	168

TABLE IX. Parameters of Raman-active modes with B_{2g} symmetry obtained from density functional theory calculations in comparison with literature. S_{RA} is Raman scattering activity. Mode frequencies of various origins reported in the literature but not corresponding to any expected frequencies were omitted. References given in second column as follows: (a) This work, LDA-DFT; (b) Ref. [5], room temperature; (c) Ref. [11], room temperature; (d) Ref. [12], room temperature; (e) Ref. [12], 21 K; (f) Ref. [9], 31–500 K.

Parameter	Ref.	$l=1$	2	3	4	5
$S^{B_{2g}}_{RA,l}$(Å^4/amu)	a	0.089	22.17	17.95	0.001	1.775
$\omega^{B_{2g}}_{RA,l}$ (cm^{-1})	a	701.1	456.7	417.4	330.8	151.9
$\omega^{B_{2g}}_{RA,l}$ (cm^{-1})	b		461			144
$\omega^{B_{2g}}_{RA,l}$ (cm^{-1})	c		459			142
$\omega^{B_{2g}}_{RA,l}$ (cm^{-1})	d		463	405	334	144
$\omega^{B_{2g}}_{RA,l}$ (cm^{-1})	e		466	412	336	146
$\omega^{B_{2g}}_{RA,l}$ (cm^{-1})	f		463	405	334	144

TABLE X. Parameters of Raman-active modes with B_{3g} symmetry obtained from density functional theory calculations in comparison with the literature. S_{RA} is Raman scattering activity. Mode frequencies of various origins reported in the literature but not corresponding to any expected frequencies were omitted. References given in second column as follows: (a) This work, LDA-DFT; (b) Ref. [5], room temperature; (c) Ref. [11], room temperature; (d) Ref. [12], room temperature; (e) Ref. [12], 21 K; (f) Ref. [9], 31–500 K.

Parameter	Ref.	$l=1$	2	3	4	5	6	7
$S^{B_{3g}}_{RA,l}$(Å^4/amu)	a	0.001	0.232	6.768	3.561	41.64	0.555	0.063
$\omega^{B_{3g}}_{RA,l}$ (cm^{-1})	a	676.6	518.6	443.6	370.2	230.7	159.3	113.0
$\omega^{B_{3g}}_{RA,l}$ (cm^{-1})	b				362	213	151	110
$\omega^{B_{3g}}_{RA,l}$ (cm^{-1})	c			448	361.5	212.5	151	
$\omega^{B_{3g}}_{RA,l}$ (cm^{-1})	d			449	363	214	153	
$\omega^{B_{3g}}_{RA,l}$ (cm^{-1})	e			453	365	219	155	
$\omega^{B_{3g}}_{RA,l}$ (cm^{-1})	f			449	363	214	153	

C. Transverse and longitudinal optical modes

Two separate sets of eigenmodes (transverse optical; TO: $\omega=\omega_{\mathrm{TO},l}$, longitudinal optical; LO: $\omega=\omega_{\mathrm{LO},l}$) and corresponding eigendisplacement unit vectors ($\hat{\mathbf{e}}_{\mathrm{TO},l}$, $\hat{\mathbf{e}}_{\mathrm{LO},l}$) can be defined from the dielectric tensor (ε) and dielectric loss tensor (ε^{-1}) [26–28], respectively,

$$|\det\{\varepsilon(\omega=\omega_{\mathrm{TO},l})\}|\rightarrow\infty, \tag{1a}$$

$$|\det\{\varepsilon^{-1}(\omega=\omega_{\mathrm{LO},l})\}|\rightarrow\infty, \tag{1b}$$

$$\varepsilon^{-1}(\omega=\omega_{\mathrm{TO},l})\hat{\mathbf{e}}_{\mathrm{TO},l}=0, \tag{1c}$$

$$\varepsilon(\omega=\omega_{\mathrm{LO},l})\hat{\mathbf{e}}_{\mathrm{LO},l}=0, \tag{1d}$$

where l is an index for multiple frequencies in the sets.

For materials with orthorhombic crystal symmetry, crystal unit cell axes **a**, **b**, and **c** are orthogonal, and wavelength-independent rotations exist, which can bring tensors ε^{-1} and ε^{-1} into diagonal form:

$$\varepsilon=\begin{pmatrix}\varepsilon_{\mathrm{a}} & 0 & 0\\ 0 & \varepsilon_{\mathrm{b}} & 0\\ 0 & 0 & \varepsilon_{\mathrm{c}}\end{pmatrix}, \tag{2}$$

$$\varepsilon^{-1}=\begin{pmatrix}\varepsilon_{\mathrm{a}}^{-1} & 0 & 0\\ 0 & \varepsilon_{\mathrm{b}}^{-1} & 0\\ 0 & 0 & \varepsilon_{\mathrm{c}}^{-1}\end{pmatrix}. \tag{3}$$

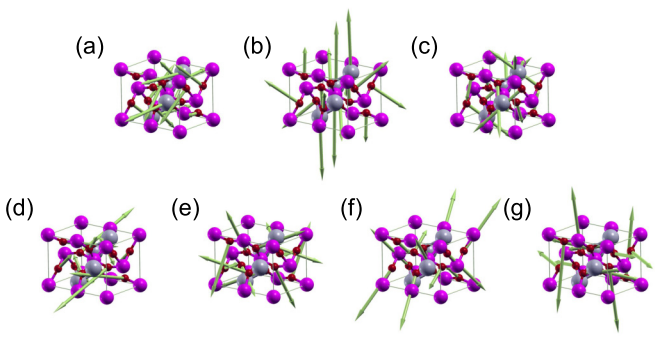

FIG. 6. Raman-active phonon modes with A_g symmetry.

Thus, Eqs. (1) simplify as

$$\varepsilon_j(\omega=\omega_{\mathrm{TO}j,l})\rightarrow\infty, \tag{4a}$$

$$\varepsilon_j^{-1}(\omega=\omega_{\mathrm{LO}j,l})\rightarrow\infty, \tag{4b}$$

$$\hat{\mathbf{e}}_{\mathrm{TO}j,l}\ ||\ \hat{\mathbf{e}}_j, \tag{4c}$$

$$\hat{\mathbf{e}}_{\mathrm{LO}j,l}\ ||\ \hat{\mathbf{e}}_j, \tag{4d}$$

with $j=\mathbf{a},\mathbf{b},\mathbf{c}$. The index l numerates phonon modes from highest to lowest frequency in order of appearance. Thereby, 3 mode series are distinguished by unit vectors polarized along one of the unit crystal axes. The total number of modes in each series, $2N_j$, is to be determined by experiment and theory. Each series contains equal sets of TO and LO modes, and in each series with ascending frequency a TO mode always precedes exactly one LO mode.

D. Generalized ellipsometry

Generalized spectroscopic ellipsometry (GSE) [29] is a contactless and nondestructive optical measurement technique that utilizes the change in polarization of *s*- and *p*-polarized light after interaction with a material. GSE allows for determination of the complex-valued spectrally dependent dielectric tensor of any arbitrary material by obtaining the 4×4 real-valued Mueller matrix, which connects the incoming and outgoing Stokes vector components according to

$$\begin{pmatrix}S_0\\S_1\\S_2\\S_3\end{pmatrix}_{\mathrm{out}}=\begin{pmatrix}M_{11} & M_{12} & M_{13} & M_{14}\\ M_{21} & M_{22} & M_{23} & M_{24}\\ M_{31} & M_{32} & M_{33} & M_{34}\\ M_{41} & M_{42} & M_{43} & M_{44}\end{pmatrix}\begin{pmatrix}S_0\\S_1\\S_2\\S_3\end{pmatrix}_{\mathrm{in}}, \tag{5}$$

with the Stokes vectors defined as

$$\begin{pmatrix}S_0\\S_1\\S_2\\S_3\end{pmatrix}=\begin{pmatrix}I_p+I_s\\ I_p-I_s\\ I_{45}-I_{-45}\\ I_{\sigma+}-I_{\sigma-}\end{pmatrix}. \tag{6}$$

This characterization technique has been used to describe long-wavelength properties in anisotropic crystals [27,28,30–32]. We have recently reported that eigendielectric displacement vector summation (EDVS) and eigendielectric loss displacement vector summation (EDLVS) approaches

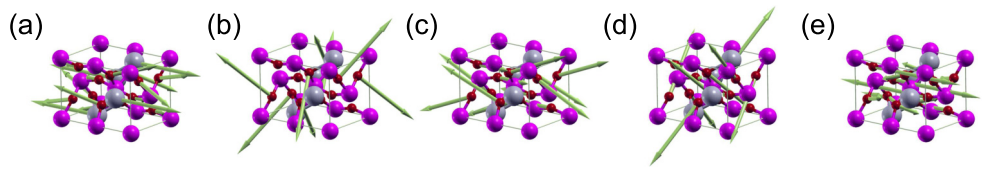

FIG. 7. Raman-active phonon modes with B_{1g} symmetry.

can be used as a physical model approach to explain and line-shape match experimentally determined dielectric function tensor elements and inverse dielectric function elements, respectively, of materials with low crystal symmetry [27,28]. We have also shown previously that the augmentation of anharmonic lifetime broadening permits the determination of broadening parameters for TO and LO modes independently [32]. These methods permit the direct determination of TO and LO mode frequencies, broadening, and amplitude parameters.

1. Ellipsometry coordinate system

The Cartesian laboratory system is defined by the ellipsometer system, where the sample surface is the x-y plane, the sample normal is the z axis pointing into the sample, and the intersection of the plane of incidence with the sample surface coincides with the x axis. The Cartesian coordinate system of the sample, $(\xi,\ \chi,\ \zeta)$, is shown in Fig. 1.

2. Physical model approach

A physical model is required to obtain meaningful and useful parameters from ellipsometric data. The ideal substrate/ambient model is utilized here assuming ideally flat and microscopically clean crystal surfaces [29,33–36]. Free parameters in this approach are the frequency-dependent complex-valued tensor elements, $\varepsilon_j(\omega)$. In addition, for every sample investigated, a set of Euler angle parameters, ϕ, θ, and ψ, is required to describe the physical rotation of the orthogonal crystal axes system relative to the laboratory axes system as explained previously by Schubert *et al.* [27].

3. Wavelength-by-wavelength analysis

Ellipsometry data from multiple samples, multiple azimuths, and multiple angles of incidence are investigated and analyzed simultaneously. In the wavelength-by-wavelength analysis approach, the parameters for the complex-valued major tensor elements ε_a, ε_b, ε_c are determined for every wavelength separately without making any assumption or conclusion from the behavior of these parameters at any other wavelength. In this wavelength-independent approach, no assumptions about specific spectral dependencies of functions $\varepsilon_j(\omega)$ are made.

4. Model dielectric function analysis

The major dielectric function tensor elements and dielectric loss function tensor elements can be rendered by summing functions in the EDVS and EDLVS approaches, respectively [27,28,30–32],

$$\varepsilon_j = \varepsilon_{\infty,j} + \sum_{l=1}^{N_j} \varrho_{\mathrm{TO},l}, \tag{7a}$$

$$\varepsilon_j^{-1} = \varepsilon_{\infty,j}^{-1} - \sum_{l=1}^{N_j} \varrho_{\mathrm{LO},l}, \tag{7b}$$

with $j = \mathbf{a}, \mathbf{b}, \mathbf{c}$. Parameters $\varepsilon_{\infty,j}$ are the high-frequency dielectric constants for polarization along crystal axes ($\mathbf{a}$, $\mathbf{b}$, $\mathbf{c}$). In order to describe the dispersions induced by TO and LO modes in Eqs. 7(a) and 7(b), respectively, we utilize anharmonic Lorentzian-broadened oscillator functions:

$$\varrho_{k,l}(\omega) = \frac{A_{k,l}^2 - i\Gamma_{k,l}\omega}{\omega_{k,l}^2 - \omega^2 - i\omega\gamma_{k,l}}, \tag{8}$$

where $A_{k,l}$, $\omega_{k,l}$, $\gamma_{k,l}$, and $\Gamma_{k,l}$ are amplitude, resonance frequency, harmonic broadening, and anharmonic broadening parameters for TO ($k = \mathrm{TO}$) or LO ($k = \mathrm{LO}$) mode l, respectively [28,32].

Additionally, in order to reduce correlations and improve sensitivity we use a second method, which ties the two independent summation approach equations together. We utilize a factorized form of the dielectric function for long-wavelength-active lattice modes. This method was previously described by Berreman and Unterwald [37] and by Lowndes [38]. The four-parameter semiquantum (FPSQ) model suggested by Gervais and Periou [39] identifies $\gamma_{\mathrm{LO},l}$, which is not necessarily equal to $\gamma_{\mathrm{TO},l}$. The difference in LO and TO mode broadening parameters accounts for the different lifetime broadening parameters of LO modes in comparison to those of their

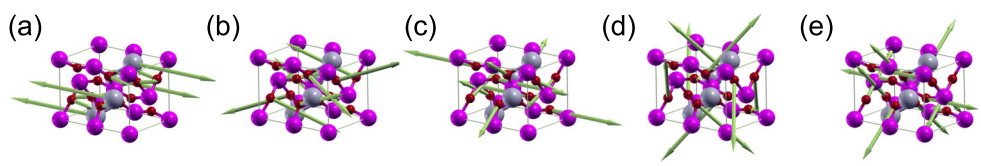

FIG. 8. Raman-active phonon modes with B_{2g} symmetry.

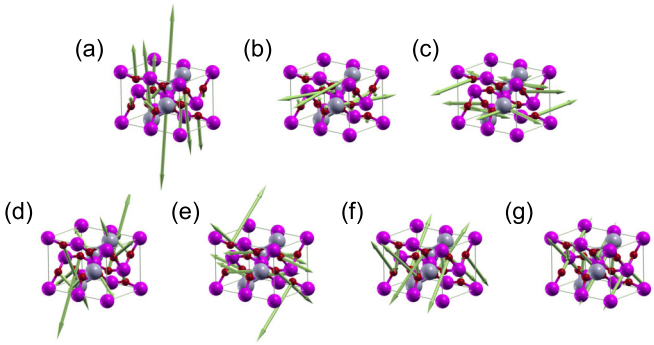

FIG. 9. Raman-active phonon modes with B_{3g} symmetry.

associated TO modes [28,30–32,39,40],

$$\varepsilon_j(\omega) = \varepsilon_{\infty,j} \prod_{l=1}^{N_j} \frac{\omega_{\mathrm{LO},l}^2 - \omega^2 - i\omega\gamma_{\mathrm{LO},l}}{\omega_{\mathrm{TO},l}^2 - \omega^2 - i\omega\gamma_{\mathrm{TO},l}}, \tag{9}$$

with $j = \mathbf{a}, \mathbf{b}, \mathbf{c}$.

5. Lyddane-Sachs-Teller relationships

Equation (9) can be used to express the Lyddane-Sachs-Teller (LST) relationship for materials with orthorhombic symmetry and multiple phonon mode branches [34,41,42], by setting $\omega = 0$,

$$\frac{\varepsilon_{\mathrm{DC},j}}{\varepsilon_{\infty,j}} = \prod_{l=1}^{N_j} \frac{\omega_{\mathrm{LO},l}^2}{\omega_{\mathrm{TO},l}^2}, \tag{10}$$

with $j = \mathbf{a}, \mathbf{b}, \mathbf{c}$. The LST relationships, 3 in the case of orthorhombic $NdGaO_3$, can be used to calculate either the static or the high-frequency value of the dielectric functions if all respective lattice mode parameters are known. In GSE analysis, the high-frequency dielectric constant parameter is usually determined as a best-model calculated parameter, and then the static constant parameters are calculated via the LST relations. However, alternatively, one may express the high-frequency parameter as a function of the static parameter and the lattice mode parameter and then the static parameter can be obtained as a best-match model parameter.

III. EXPERIMENT

Three 10 mm × 10 mm × 0.5 mm single-crystal samples of $NdGaO_3$, polished on one side, were purchased from MTI Corporation [43] with surface cuts of (110), (101), and (001). Mueller matrix data were obtained subsequently from each sample surface at five azimuthal orientations, rotated clockwise in 45° increments. Data were taken from two angles of incidence ($\varphi = 50°$ and 70°). Data were taken at room temperature by infrared (IR) and far-infrared (FIR) GSE. The IR-GSE measurements were performed on a rotating compensator infrared ellipsometer (J. A. Woollam Co., Inc.) in the spectral range of ≈250–8000 cm^{-1} with a spectral resolution of 2 cm^{-1}. The FIR-GSE measurements were performed using our in-house-built rotating-polarizer rotating-analyzer GSE instrument in the spectral range of 30–650 cm^{-1} with an average spectral resolution of 2 cm^{-1} [44]. Data in the spectral overlap region are in excellent agreement. For analysis, data from the FIR instrument from 80–500 cm^{-1} were combined with data from the IR instrument from 500–1200 cm^{-1}. All Mueller matrix elements are normalized to element M_{11}. Note that due to the lack of a compensator for the FIR range in this work, no elements of the fourth row or column are reported for the FIR range. Data included for analysis of the fourth-row elements are obtained from the IR instrument in the range of 250–1200 cm^{-1}. Data obtained from all rotations are included in the analysis; however, only three azimuthal orientations are discussed and shown here for brevity. Note that M_{44} is not obtained due to a lack of two compensators in both instrument setups. In accordance with the orthorhombic crystal symmetry, regardless of the sample surface orientation, measurements from azimuthally rotated orientations 180° apart were observed to be identical. All model calculations were performed using WVASE32 (J. A. Woollam Co., Inc.).

IV. RESULTS AND DISCUSSION

A. Mueller matrix analysis

Experimental and best-match model calculated Mueller matrix are shown in Figs. 10–12. Insets within each figure show crystallographic axes orientation for each of the (110), (101), and (001) surfaces. The upper half of the Mueller matrix is presented with individual elements arranged in panels in which symmetric elements $M_{ij} = M_{ji}$ are plotted within the same panel. All elements are normalized to M_{11}. Data collected from three azimuthal orientations (P1, P2, and P3) as well as two angles of incidence ($\Phi_a = 50°$ and 70°) are shown.

Effects due to coupling between *p*- and *s*-polarized incident electromagnetic waves are clearly observed in off-block diagonal elements (i.e., M_{13}, M_{14}, M_{23}, M_{24}). These elements contain nonzero data whenever crystallographic axes of noncubic materials are oriented nonparallel to the Cartesian ellipsometer coordinate axes, and at wave numbers at which the dielectric function tensor is isotropic. At so-called "pseudoisotropic" points, for example, in position P3 of Fig. 10, the off-block diagonal Mueller matrix elements of anisotropic materials become zero regardless of wave number due to the lineup of crystallographic axes with the ellipsometer coordinate axes. As discussed further below, vertical lines in Figs. 10–12 indicate the spectral positions of TO (solid) and LO (dotted) lattice modes polarized along the **a** axis (dark cyan), **b** axis (orange), and **c** axis (violet), as identified from our best-match model analysis.

Data from all surfaces, orientations, and angles of incidence were analyzed simultaneously for each wavelength. This wavelength-by-wavelength analysis utilizes 15 independent parameters including the real and imaginary parts of the dielectric function in each direction ($\varepsilon_{\mathbf{a}}$, $\varepsilon_{\mathbf{b}}$, and $\varepsilon_{\mathbf{c}}$), as well as the 9 Euler angles describing the orientation of each sample. We note the excellent agreement between the Mueller matrix data (green) and the wavelength-by-wavelength model rendered data (red) shown in Figs. 10–12. The tensor elements of the dielectric function (ε) and the dielectric loss function (ε^{-1}) determined by this wavelength-by-wavelength analysis technique are shown in Figs. 13–15 as green symbols. We note

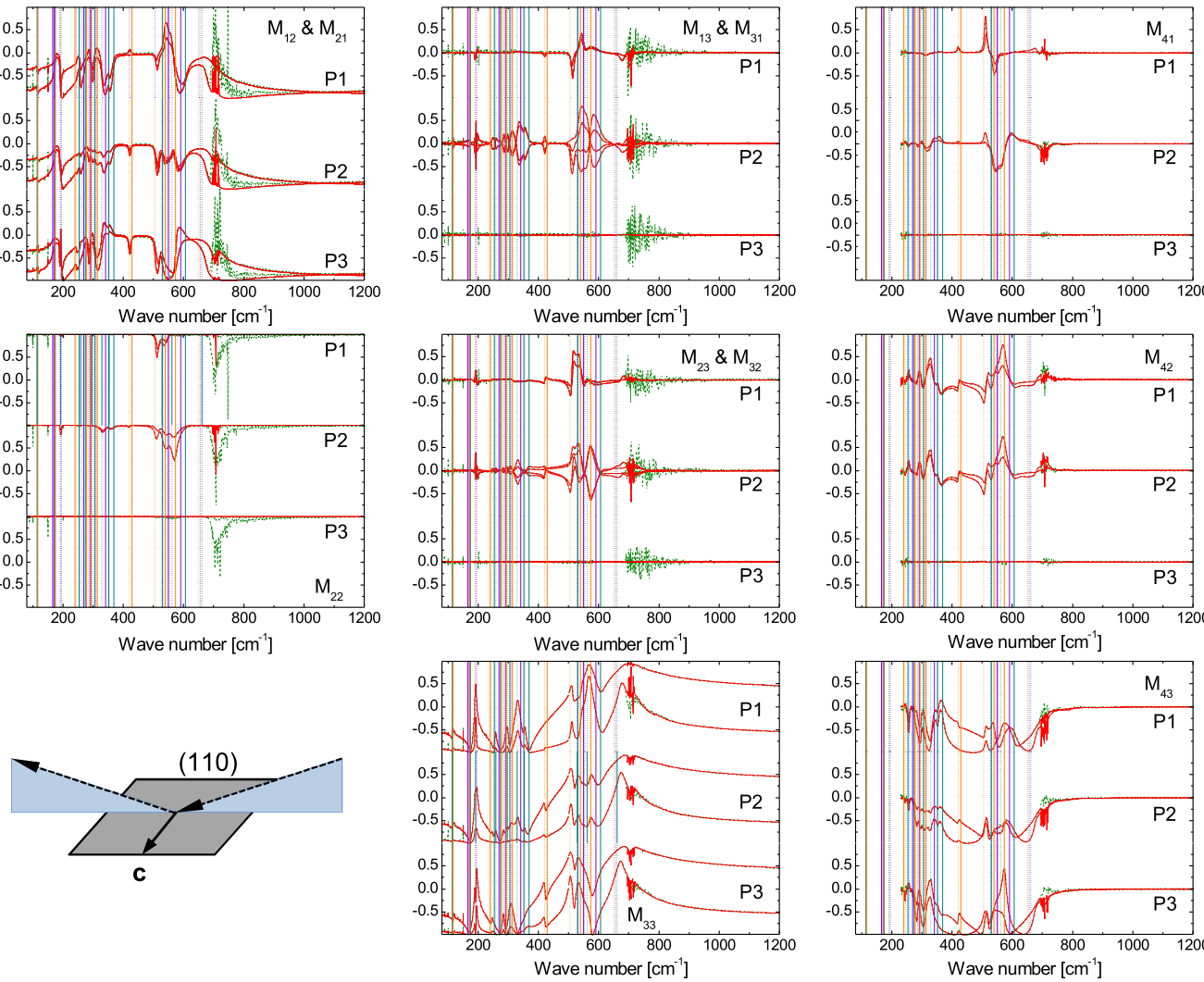

FIG. 10. Experimental (dotted, green lines) and best-match model calculated (solid, red lines) normalized Mueller matrix data obtained from the (110) sample surface at three selected azimuthal orientation angles P1, P2, and P3 [$\varphi = -90.(1)$, $\varphi = -45.(1)$, and $\varphi = -0.(1)$, respectively]. Data were taken at two angles of incidence ($\Phi_a = 50^\circ$ and 70°). Mueller matrix data symmetric in their indices are plotted within the same panels, for convenience. Vertical lines indicate positions of TO (solid lines) and LO (dotted lines) modes with colors corresponding to crystal axes. Fourth-row elements are limited to approximately 230 cm^{-1} due to a lack of compensator in the FIR spectral region. All Mueller matrix elements are normalized to M_{11}. The remaining two Euler angle parameters determined to describe this sample are $\theta = 89.(8)$ and $\psi = 54.(1)$, which are consistent with the crystallographic orientation of the (110) surface. The inset schematically depicts the sample surface as well as the plane of incidence and the orientation of crystallographic axis **c** at P3.

that the dielectric loss tensor elements were determined by numerically inverting the experimentally determined complex-valued dielectric function tensor, and thus we obtain a negative imaginary part of the dielectric loss function. The samples were undoped and thus no free charge carrier contributions were observed.

B. Anisotropic static and high-frequency dielectric constants

Static and high-frequency dielectric constants along each crystal axis determined in our GSE analysis are given in Table XI. Values predicted by our DFT calculations are given for comparison. Experimentally determined $\varepsilon_{\infty,j}$ values are lower than DFT-calculated values; however, the same trend of $\varepsilon_{\infty,\mathbf{c}} > \varepsilon_{\infty,\mathbf{a}} > \varepsilon_{\infty,\mathbf{b}}$ is observed. The values of the DFT-calculated static dielectric constants $\varepsilon_{\mathrm{DC},j}$ are slightly lower than those determined by GSE. While again the trend between the two methods is observed to be the same with $\varepsilon_{\mathrm{DC},\mathbf{a}} > \varepsilon_{\mathrm{DC},\mathbf{c}} > \varepsilon_{\mathrm{DC},\mathbf{b}}$, the error bars on the GSE-determined values are larger in this case.

High-frequency dielectric constants have been reported in the literature and are included in Table XI for comparison. Höfer *et al.* [10] and Suda *et al.* [13] provide the anisotropic high-frequency dielectric tensor with values along the three crystallographic directions determined from analysis of reflectivity data. Zhang *et al.* [7] also provided a high-frequency dielectric constant; however the crystal axis assignment was unclear in Ref. [7]. The static dielectric tensor was only provided by Suda *et al.* [13] with values along each of the three crystallographic axes and with values considerably

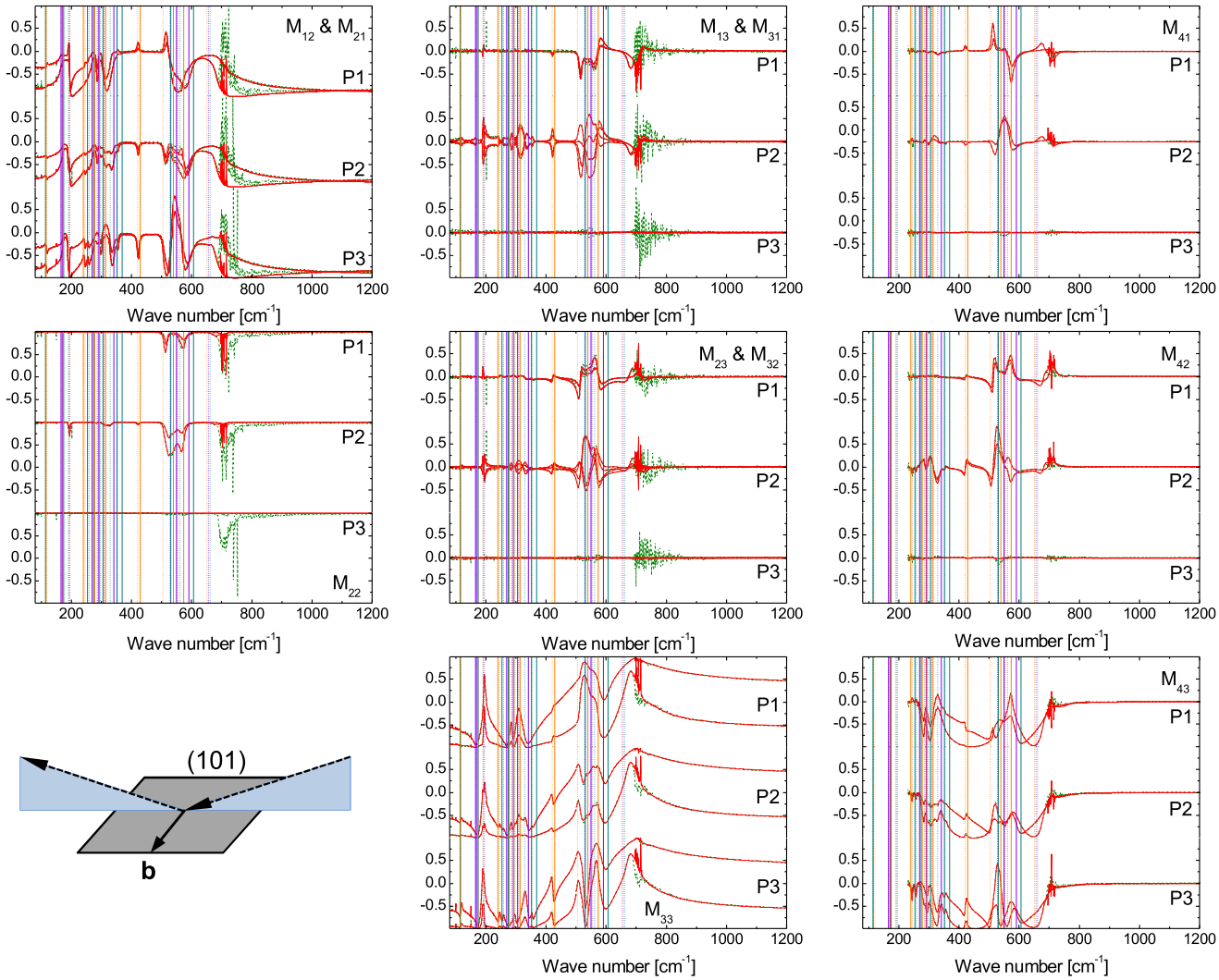

FIG. 11. Same as Fig. 10 for a (101) sample at azimuthal orientations P1, P2, and P3 [$\varphi = 0.(7)$, $\varphi = 45.(7)$, and $\varphi = 90.(7)$, respectively]. Euler angles $\theta = -44.(4)$ and $\psi = -89.(7)$ are consistent with the crystallographic orientation of the (101) surface. The inset schematically depicts the sample surface as well as the plane of incidence and the orientation of crystallographic axis **b**, shown approximately for position P3.

higher than we find in this work both experimentally and theoretically.

C. TO and LO mode analysis

The real and imaginary parts of the dielectric function rendered using Eqs. (7) and (8) along each crystallographic **a** axis ($\varepsilon_{\mathbf{a}}$), **b** axis ($\varepsilon_{\mathbf{b}}$), and **c** axis ($\varepsilon_{\mathbf{c}}$) are shown in Fig. 13(a), Fig. 14(a), and Fig. 15(a), respectively. TO modes are identified as the maxima in the imaginary parts of the dielectric function and the line shapes were matched by utilizing Eq. 7(a) and Eq. (8). Frequencies of the 9 TO phonon modes polarized along the **a** axis determined from our model dielectric function analysis are shown as vertical orange solid lines in Fig. 13(a). Similarly in Fig. 14(a) and Fig. 15(a), frequencies of the 7 TO phonon modes polarized along the **b** axis and the 9 TO phonon modes polarized along the **c** axis are depicted as violet and dark cyan solid lines, respectively. Bar graphs are shown in the upper panel corresponding to the phonon mode amplitudes and frequencies found in the DFT analysis. Note that some weak modes have been magnified for convenience.

Similarly, the real and imaginary parts of the dielectric loss function, or the inverse dielectric functions, along the crystallographic **a** axis ($\varepsilon_{\mathbf{a}}^{-1}$), **b** axis ($\varepsilon_{\mathbf{b}}^{-1}$), and **c** axis ($\varepsilon_{\mathbf{c}}^{-1}$) are shown in Fig. 13(b), Fig. 14(b), and Fig. 15(b), respectively. LO modes are identified as the maxima in the imaginary parts of the dielectric loss function and the line shapes were matched by utilizing Eq. 7(b) and Eq. (8). Frequencies of the 9 LO phonon modes polarized along the **a** axis determined from our model dielectric function analysis are shown as vertical orange dotted lines in Fig. 13(a). Similarly in Figs. 14(a) and 15(a), frequencies of the 7 LO phonon modes polarized along the **b** axis and the 9 LO phonon modes polarized along the **c** axis are depicted as violet and dark cyan dotted lines, respectively. DFT analysis resulting amplitudes and frequencies are presented for LO modes in the upper panel. Again several modes were magnified for ease of view.

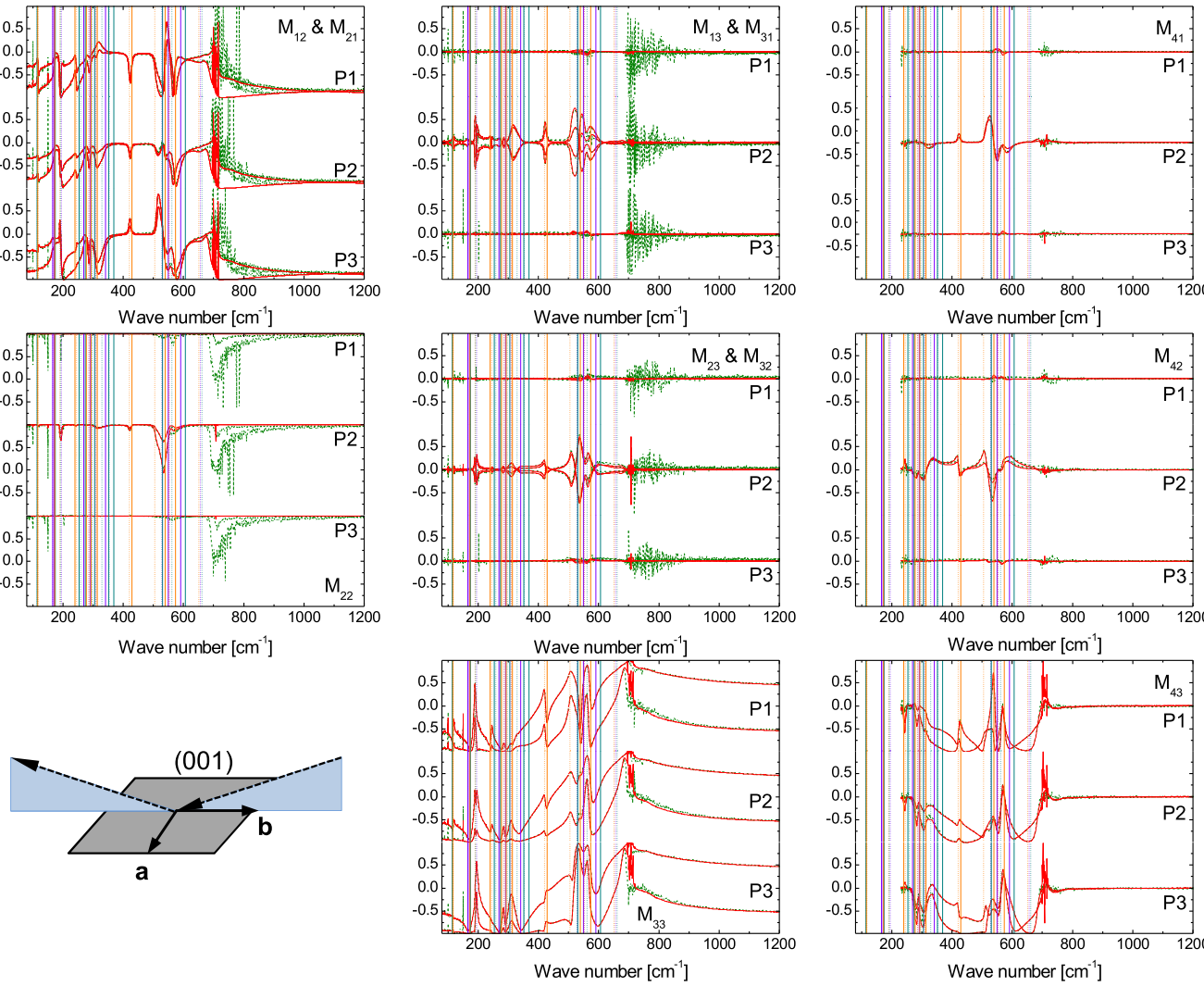

FIG. 12. Same as Fig. 10 for a (001) sample at azimuthal orientations P1, P2, and P3 [$\varphi = 5(6)$, $\varphi = 10(1)$, and $\varphi = 14(6)$, respectively]. Euler angles $\theta = -2.(7)$ and $\psi = -5(7)$ are consistent with the crystallographic orientation of the (001) surface. The inset schematically depicts the sample surface as well as the plane of incidence and the orientation of crystallographic axes **a** and **b**, shown approximately for position P3. Note that due to the small inclination of axis **c** from the surface normal, Euler angles φ and ψ are highly correlated, since for $\theta = 0$ both φ and ψ perform the same rotations.

Resulting parameter values ($A_{TO,l}$, $\omega_{TO,l}$, $\gamma_{TO,l}$, $\Gamma_{TO,l}$, $A_{LO,l}$, $\omega_{LO,l}$, $\gamma_{LO,l}$, and $\Gamma_{LO,l}$) determined in our GSE model dielectric function analysis for each tensor element are presented in Tables IV–VI. Several weak modes or modes partially subsumed into shoulders of stronger modes were identified and fitted locally for increased sensitivity. Frequencies and amplitude parameters compare well with DFT calculations. All 25 predicted infrared-active TO and LO phonon mode pairs were identified by GSE.

We compare our results with literature values of experimentally identified long-wavelength-active TO and LO modes by reflectivity measurements. Höfer *et al.* [10] identified the full set of 9 TO and LO mode pairs with B_{2u} symmetry oriented along the **a** axis. Frequency parameters of TO and LO modes with B_{2u} symmetry identified in this work agree very well, only varying by a few cm^{-1}. However, an additional oscillator oriented along axis **a** was introduced in the analysis by Höfer *et al.*, which does not correspond to any feature or phonon mode identified in our work. Suda *et al.* experimentally identified 8 TO modes with B_{2u} symmetry, which agree well with our 8 highest-frequency modes. The ninth expected TO mode was unidentified and none of the LO modes were identified.

Of the 7 expected TO and LO mode pairs with B_{3u} symmetry oriented along the crystallographic **b** axis, Höfer *et al.* found 5 modes, which correspond to our mode pairs with $l = 1, 3, 4, 5, 6$, which agree within a few cm^{-1}. TO modes for the same 5 modes were observed by Suda *et al.*, however, with significantly different frequencies in some cases.

For mode pairs with B_{1u} symmetry Höfer *et al.* identified 7 of the 9 TO and LO modes expected along the **c** axis. Höfer *et al.* identified TO modes corresponding to our modes with $l = 1, 3, 4, 5, 6, 7, 8$ and the LO modes correspond to modes with $l = 1, 2, 4, 5, 6, 7, 8$ with excellent agreement. Erroneously, in the analysis by Höfer *et al.* a TO mode at

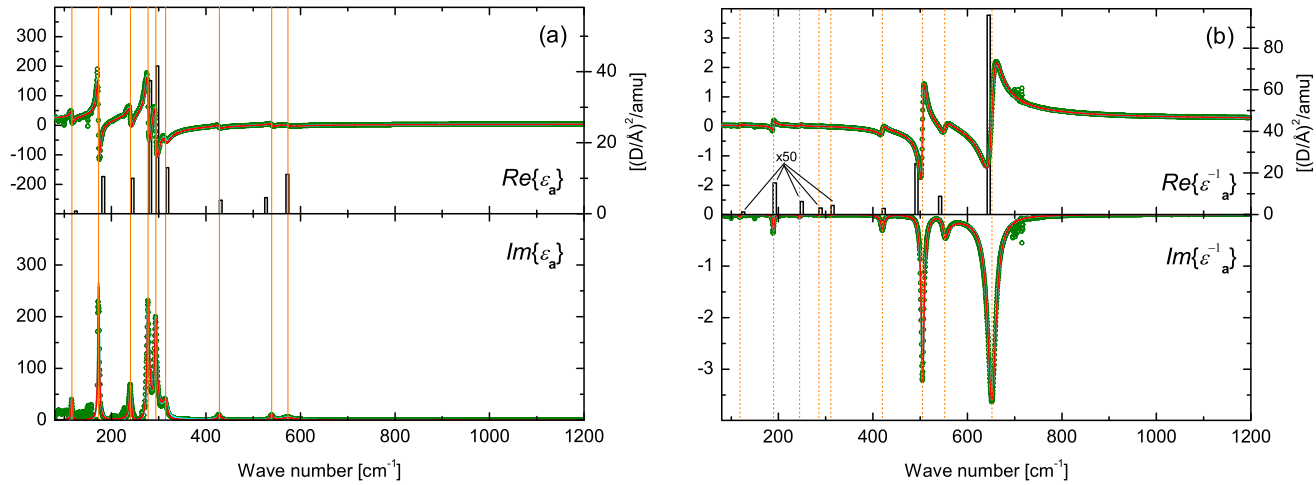

FIG. 13. (a) Dielectric function tensor element $\varepsilon_{\mathbf{a}}$ and (b) dielectric loss tensor element $\varepsilon_{\mathbf{a}}^{-1}$. Green symbols indicate results from wavelength-by-wavelength best-match model regression analysis matching the experimental Mueller matrix data shown in Figs. 10–12. Red solid lines are the resulting line shapes corresponding to the analysis using Eqs. (7) and (8) for the dielectric function and dielectric loss function, respectively. Vertical lines in (a) and (b) indicate resulting TO and LO frequencies, respectively. Vertical bars show long-wavelength transition dipole moments in atomic units calculated by DFT.

367 cm^{-1} was paired with an LO mode at 563 cm^{-1}, since the TO mode with $l = 2$ and the LO mode with $l = 3$ were unidentified. Additionally the mode pair with $l = 9$ was not observed by Höfer *et al.* Suda *et al.* also identified 7 TO modes by experiment with reasonable agreement for those centered at lower wave number but significantly shifted center frequencies for those at higher wave number.

Zhang *et al.* [7] investigated only a single orientation of a (100) NGO single crystal and identified 13 TO modes but did not describe polarization, and thus cannot be compared here. Additionally, no LO modes were identified.

We find agreement with the previously described broadening rule generalized for anisotropic materials with multiple modes shown by Schubert, Tiwald, and Herzinger [30]. This rule states that for each direction in an anisotropic material, in order to maintain physical interpretation, the sum of all LO broadening parameters must be larger than the sum of all TO broadening parameters, which is satisfied for our analysis of $NdGaO_3$ here.

D. Raman-active modes

There exist many detailed studies of Raman-active modes in $NdGaO_3$. The comparison of phonon frequencies of Raman-active modes from selected literature with the parameters calculated using DFT in this work are given in Tables VII–X. We restrict this comparison to the relevant modes only, i.e., modes active in the conventional Raman scattering process. Kamishima *et al.* [12] in their tables with Raman frequencies also included modes deduced from temperature-dependent optical absorption and photoluminescence measurements. These frequencies, however, do not match any of our calculated Raman-active modes

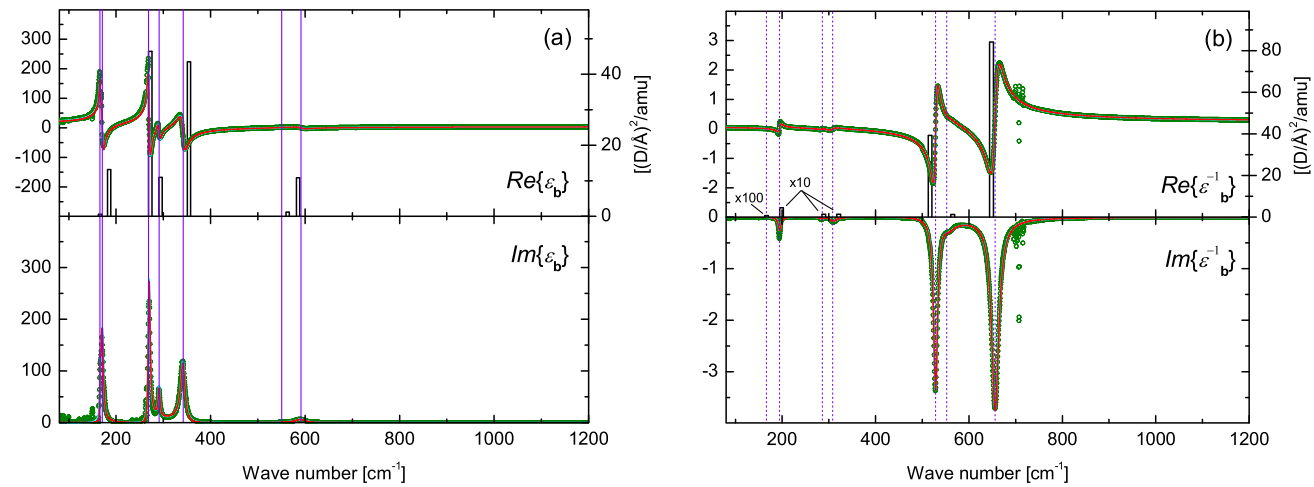

FIG. 14. Same as for Fig. 13 but for $\varepsilon_{\mathbf{b}}$ and $\varepsilon_{\mathbf{b}}^{-1}$ for polarization along the **b** axis.

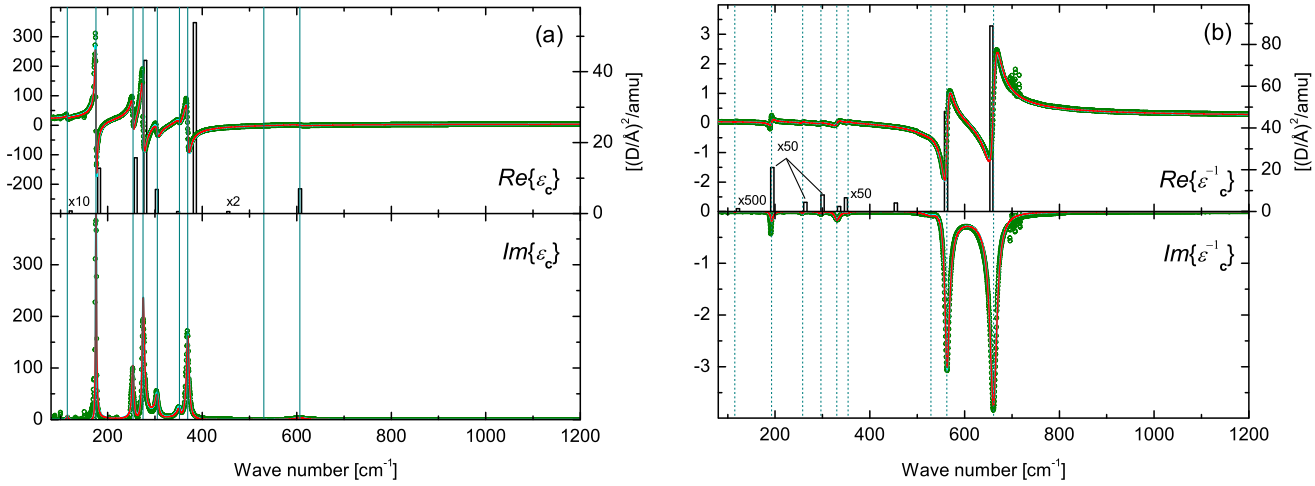

FIG. 15. Same as for Fig. 13 but for $\varepsilon_{\mathbf{c}}$ and $\varepsilon_{\mathbf{c}}^{-1}$ for polarization along the **c** axis.

and we consider them outside the scope of the current paper. For the phonon modes that can be unambiguously matched, the calculated and observed experimental frequencies agree to within a few cm^{-1}. Several high-frequency modes of B_{1g}, B_{2g}, and B_{3g} symmetry have not been observed experimentally so far. Based on the fact that all the phonon modes for which there are available high-quality experimental data are reproduced in our DFT calculations with excellent accuracy, we have no reason to expect the remaining few that so far were not observed to be any less accurate. They will undoubtedly be identified in future experiments.

TABLE XI. Anisotropic high-frequency dielectric constants and static dielectric constants along crystal axes **a**, **b**, and **c** determined in this work by GSE using the LST relations [Eq. (10)] and DFT in comparison with selected values from the literature. The last digit is determined within the 90% confidence interval, which is indicated with parentheses for each parameter. Literature data have been converted to the *Pnma* cell used in the present study.

	Reference	$j = \mathbf{a}$	**b**	**c**
$\varepsilon_{\infty,j}$	This work (GSE)	4.30(9)	4.08(1)	4.41(7)
$\varepsilon_{\infty,j}$	This work (DFT)	4.87	4.77	4.98
$\varepsilon_{\mathrm{DC},j}$	This work (GSE)	22.(7)	21.(1)	21.(7)
$\varepsilon_{\mathrm{DC},j}$	This work (DFT)	20.8	19.4	20.6
$\varepsilon_{\infty,j}$	Höfer *et al.* [10]	4.04	4.22	4.26
$\varepsilon_{\infty,j}$	Zhang *et al.* [7]	4.1[a]		
$\varepsilon_{\infty,j}$	Suda *et al.* [13]	4.1	4.0	4.0
$\varepsilon_{\mathrm{DC},j}$	Suda *et al.* [13]	29.7	24.6	25

[a]Crystal axis assignment unclear.

E. Phonon dispersion

Figure 16(a) shows the complete phonon dispersion along a high-symmetry path through the first Brillouin zone, for all 60 phonon modes (including the acoustic and silent phonons). Comparing with the phonon dispersion presented by Suda *et al.* [9,13], we can observe that the DFT-calculated phonons exhibit higher dispersion. Most notably, the entire branch above 600 cm^{-1} is missing in the plot of Suda *et al.* In our DFT results, this branch, close to the Γ point, includes three highest-frequency Raman modes, one each of B_{1g}, B_{2g}, and B_{3g} symmetry, and one LO mode, with symmetry depending on the direction of approaching the Γ point. As mentioned above these three high-frequency Raman-active modes have not been reported so far, and hence were not included in Suda *et al.*'s calculations of the interatomic force fields. In fact, no phonon mode in Table II of Ref. [9] exceeds the frequency of 600 cm^{-1}. The same is mainly true for their refined model published in Ref. [13], with the exception of one model-calculated frequency of the highest silent A_u mode (610.30 cm^{-1}) that actually falls quite close to the highest-

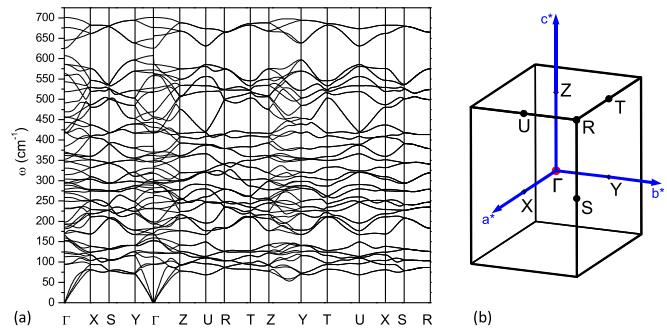

FIG. 16. (a) Phonon dispersion along a high-symmetry path through the Brillouin zone. (b) The corresponding Brillouin zone with high-symmetry points marked. a^*, b^*, and c^* denote axes in the reciprocal space. Sketch prepared using XCrysDen [24].

frequency A_u mode calculated from first principles in the current work (585.84 cm^{-1}).

V. CONCLUSIONS

Plane-wave DFT calculations of long-wavelength-active Γ-point phonon frequencies of $NdGaO_3$ using the LDA exchange correlation functional of Perdew and Wang (PW) [15] lead to excellent agreement with a vast set of information obtained from experimental data analyses. Measurement of the frequency-dependent dielectric function tensor and dielectric loss tensor of orthorhombic neodymium gallium oxide in the spectral range 80–1200 cm^{-1} permits comparison with accurate and highly precise infrared-active lattice modes. The high number of participating atoms in the unit cell leads to the complex Γ-point phonon displacement pattern displayed here in graphic images. The full phonon dispersion based on the DFT-calculated interatomic force field constants may become useful for evaluation of thermal transport or luminescence properties, for example. The dielectric summation and dielectric loss summation model approaches previously suggested for low-symmetry crystals and augmented by effects due to lattice anharmonicity are fully suitable to describe the experimentally determined dielectric function tensor elements for the single-crystalline centrosymmetric neodymium gallate. Use of the Lyddane-Sachs-Teller relation together with the results from the dielectric summation and dielectric loss summation model approaches enables the prediction of highly accurate and precise anisotropic static dielectric constants, and comparison among DFT, ellipsometry, and literature information leads to satisfactory agreement. The agreement between experimentally determined Raman-active modes and DFT-calculated modes is excellent, and modes predicted but not yet measured may serve as guidance for future experiments.

ACKNOWLEDGMENTS

This work was supported in part by the National Science Foundation under Award No. DMR 1808715, by the Air Force Office of Scientific Research under Award No. FA9550-18-1-0360, and by the Nebraska Materials Research Science and Engineering Center under Award No. DMR 1420645. We acknowledge support from the Swedish Energy Agency under Award No. P45396-1, the Swedish Research Council VR under Award No. 2016-00889, the Swedish Foundation for Strategic Research under Grants No. FL12-0181, No. RIF14-055, and No. EM16-0024, and the Swedish Government Strategic Research Area in Materials Science on Functional Materials at Linköping University, Faculty Grant SFO Mat LiU No. 2009-00971. M.S. acknowledges the University of Nebraska Foundation and the J. A. Woollam Foundation for financial support. Density functional theory calculations were performed at the Holland Computing Center of the University of Nebraska, which receives support from the Nebraska Research Initiative.

[1] H. Takahashi, J. Ohta, H. Fujioka, and M. Oshima, Thin Solid Films **407**, 114 (2002).

[2] H. Okazaki, A. Arakawa, T. Asahi, O. Oda, and K. Aiki, Solid-State Electron. **41**, 263 (1997).

[3] A. H. Reshak, M. Piasecki, S. Auluck, I. V. Kityk, R. Khenata, B. Andriyevsky, C. Cobet, N. Esser, A. Majchrowski, M. Świrkowicz, R. Diduszko, and W. Szyrski, J. Phys. Chem. B **113**, 15237 (2009).

[4] K. S. Gavrichev, V. E. Gorbunov, L. N. Golushina, G. A. Totorova, E. A. Tishchenko, Y. G. Nadtochii, and Y. B. Poyarkov, Neorg. Mater. **30**, 1443 (1994) [Inorg. Mater. **30**, 1346 (1994)].

[5] D. Savytskii, D. Y. Sugak, A. Suchocki, A. O. Matkovskii, I. Savytskii, V. Dzhala, and P. Kaczor, in *XII Conference on Solid State Crystals: Materials Science and Applications, Zakopane, Poland, 1996*, Solid State Crystals: Growth and Characterization (SPIE, USA, 1997), Vol. 3178, pp. 283–287.

[6] V. Orera, L. Trinkler, R. Merino, and A. Larrea, J. Phys.: Condens. Matter **7**, 9657 (1995).

[7] Z. Zhang, B. Choi, M. Flik, and A. C. Anderson, J. Opt. Soc. Am. B **11**, 2252 (1994).

[8] M. C. Saine, E. Husson, and H. Brusset, Spectrochim. Acta, Part A **38**, 19 (1982).

[9] J. Suda, T. Mori, H. Saito, O. Kamishima, T. Hattori, and T. Sato, Phys. Rev. B **66**, 174302 (2002).

[10] S. Höfer, R. Uecker, A. Kwasniewski, J. Popp, and T. G. Mayerhöfer, Vibrational Spectroscopy **78**, 17 (2015).

[11] M. L. Sanjuán, V. M. Orera, R. I. Merino, and J. Blasco, J. Phys.: Condens. Matter **10**, 11687 (1998).

[12] O. Kamishima, H. Koyama, R. Takahashi, Y. Abe, T. Sato, and T. Hattori, J. Phys.: Condens. Matter **14**, 3905 (2002).

[13] J. Suda and T. Sato, J. Spectrosc. Soc. Jpn. **54**, 97 (2005).

[14] Quantum ESPRESSO is available from http://www.quantum-espresso.org; See also P. Giannozzi, S. Baroni, N. Bonini, M. Calandra, R. Car, C. Cavazzoni, D. Ceresoli, G. L. Chiarotti, M. Cococcioni, I. Dabo, A. D. Corso, S. de Gironcoli, S. Fabris, G. Fratesi, R. Gebauer, U. Gerstmann, C. Gougoussis, A. Kokalj, M. Lazzeri, L. Martin-Samos, N. Marzari, F. Mauri, R. Mazzarello, S. Paolini, A. Pasquarello, L. Paulatto, C. Sbraccia, S. Scandolo, G. Sclauzero, A. P. Seitsonen, A. Smogunov, P. Umari, and R. M. Wentzcovitch, J. Phys.: Condens. Matter **21**, 395502 (2009).

[15] J. Perdew and Y. Wang, Phys. Rev. B **45**, 13244 (1992); **98**, 079904(E) (2018).

[16] D. R. Hamann, Phys. Rev. B **88**, 085117 (2013).

[17] M. J. van Setten, M. Giantomassi, E. Bousquet, M. J. Verstraete, D. R. Hamann, X. Gonze, and G.-M. Rignanese, Comput. Phys. Commun. **226**, 39 (2018).

[18] L. Vasylechko, L. Akselrud, W. Morgenroth, U. Bismayer, A. Matkovskii, and D. Savytskii, J. Alloys Compd. **297**, 46 (2000).

[19] H. J. Monkhorst and J. D. Pack, Phys. Rev. B **13**, 5188 (1976).

[20] S. Baroni, S. de Gironcoli, A. D. Corso, S. Baroni, S. de Gironcoli, and P. Giannozzi, Rev. Mod. Phys. **73**, 515 (2001).

[21] M. Born and K. Huang, *Dynamical Theory of Crystal Lattices* (Clarendon, Oxford, 1954).
[22] G. Venkataraman, L. A. Feldkamp, and V. C. Sahni, *Dynamics of Perfect Crystals* (MIT Press, Cambridge, MA, 1975).
[23] X. Gonze and C. Lee, Phys. Rev. B **55**, 10355 (1997).
[24] A. Kokalj, Comput. Mater. Sci. **28**, 155 (2003); Code available from http://www.xcrysden.org.
[25] M. Marezio, J. P. Remeika, and P. D. Dernier, Inorg. Chem. **7**, 1337 (1968).
[26] M. Schubert, Phys. Rev. Lett. **117**, 215502 (2016).
[27] M. Schubert, R. Korlacki, S. Knight, T. Hofmann, S. Schöche, V. Darakchieva, E. Janzén, B. Monemar, D. Gogova, Q.-T. Thieu *et al.*, Phys. Rev. B **93**, 125209 (2016).
[28] A. Mock, R. Korlacki, S. Knight, and M. Schubert, Phys. Rev. B **97**, 165203 (2018).
[29] M. Schubert, Phys. Rev. B **53**, 4265 (1996).
[30] M. Schubert, T. E. Tiwald, and C. M. Herzinger, Phys. Rev. B **61**, 8187 (2000).
[31] S. Schöche, T. Hofmann, R. Korlacki, T. E. Tiwald, and M. Schubert, J. Appl. Phys. **113**, 164102 (2013).
[32] A. Mock, R. Korlacki, S. Knight, and M. Schubert, Phys. Rev. B **95**, 165202 (2017).
[33] M. Schubert, in *Introduction to Complex Mediums for Optics and Electromagnetics*, edited by W. S. Weiglhofer and A. Lakhtakia (SPIE, Bellingham, WA, 2004), pp. 677–710.
[34] M. Schubert, *Infrared Ellipsometry on Semiconductor Layer Structures: Phonons, Plasmons, and Polaritons*, Springer Tracts in Modern Physics Vol. 209 (Springer, Berlin, 2004).
[35] M. Schubert, in *Handbook of Ellipsometry*, edited by E. Irene and H. Tompkins (William Andrew Publishing, Norwich, 2004).
[36] H. Fujiwara, *Spectroscopic Ellipsometry: Principles and Applications* (John Wiley & Sons, New York, 2007).
[37] D. W. Berreman and F. C. Unterwald, Phys. Rev. **174**, 791 (1968).
[38] R. P. Lowndes, Phys. Rev. B **1**, 2754 (1970).
[39] F. Gervais and B. Piriou, J. Phys. C **7**, 2374 (1974).
[40] M. Schubert, T. Hofmann, C. M. Herzinger, and W. Dollase, Thin Solid Films **455–456**, 619 (2004).
[41] R. H. Lyddane, R. Sachs, and E. Teller, Phys. Rev. **59**, 673 (1941).
[42] H. Takahashi, Phys. Rev. B **11**, 1636 (1975).
[43] Note that $NdGaO_3$ single-crystalline samples purchased from MTI were described by the company using the *Pbnm* cell definition and the surface cuts were thus identified as (011), (110), and (100).
[44] P. Kühne, C. M. Herzinger, M. Schubert, J. A. Woollam, and T. Hofmann, Rev. Sci. Instrum. **85**, 071301 (2014).